PCCP

ROYAL SOCIETY OF CHEMISTRY

PAPER

View Article Online
View Journal | View Issue

Cite this: *Phys. Chem. Chem. Phys.*, 2025, **27**, 17521

X-ray photoelectron spectroscopy of surfactants on sub-micron aqueous aerosols

Alexandra M. Deal, [a] Alexander M. Prophet, [a] Sorren Warkander, [a] Madison M. Foreman, [ab] Pyeongeun Kim, [a] Daniel M. Neumark, [ab] Musahid Ahmed [a] and Kevin R. Wilson *[a]

Organic molecules at the aqueous interfaces of droplets and aerosols can influence multiphase chemistry and cloud condensation nuclei activity. While surface tension measurements on flat surfaces are commonly used to quantify organic partitioning and structure, extending these measurements to more realistic aerosols that might exist in metastable, supercooled and supersaturated states remains a challenge. Here, we use aerosol velocity map imaging X-ray photoelectron spectroscopy (A-VMI-XPS), a surface-sensitive and *in situ* technique, to study the partitioning and structure of a model surfactant (*n*-octyl β-D-thioglucopyranoside, OTG) in submicron aqueous aerosols with a mean radius of 116 nm. After accounting for finite size effects and evaporative cooling, we find the bulk concentrations of OTG in the aerosol are depleted 600-fold relative to macroscopic solutions. At the low temperatures of the experiment (*ca.* ~188 K), we obtain a Langmuir equilibrium constant of 700 m^3 mol^{-1}, which corresponds to 4.9 m^3 mol^{-1} at room temperature; a value that is consistent with prior literature reports. Analysis of photoelectron angular distributions, peak areas, and secondary electron escape barriers indicates a transition from a disordered surfactant layer at low [OTG] to a more structured layer at high [OTG]. These results link macroscopic surface tension measurements to nanoparticle surfactant behavior and demonstrate the utility of A-VMI-XPS in probing surfactant coating structure on free aerosols, with implications for understanding the impact of organic coatings on cloud formation and atmospheric chemistry.

Received 6th June 2025,
Accepted 31st July 2025

DOI: 10.1039/d5cp02126j

rsc.li/pccp

1. Introduction

Droplets and aerosols have important roles in atmospheric processes, including cloud droplet formation, new particle generation, gas uptake, heterogeneous reactions, and ice nucleation.[1] Surfactants that accumulate at the interfaces of these particles can significantly impact the role of aerosols. For example, surfactant partitioning to droplet surfaces can lower surface tension and enhance the ability of droplets to act as cloud condensation nuclei (CCN).[2–5] In addition, surfactant coatings may create interfacial barriers between liquid and gas phases, thereby affecting multiphase transport and reactivity.[6,7] Each of these processes may influence Earth's energy balance, or radiative forcing, highlighting the importance of accurately quantifying surfactant behavior—a topic that has garnered increasing attention.[8–10]

Surface tension measurements are commonly used to quantify surfactant partitioning,[8] while techniques such as reflection–absorption,[11,12] nonlinear,[13,14] and photoelectron spectroscopies[15,16] provide additional structural insights. These methods are typically applied to flat, macroscopic water surfaces, and results are often extrapolated to atmospheric droplets. Drawing insights from macroscopic surfaces can be challenging, however, since aerosols often exist in metastable, supercooled, and supersaturated states with much higher surface area-to-volume ratios—factors that recent studies suggest can significantly affect surfactant partitioning and surface tension.[2,9,10,17,18] In fact, the presence of surfactants in small droplets has been proposed as a reason for discrepancies between CCN activity predicted by Köhler theory and experimental observations.[4] Hence, there is a critical need for surface-sensitive, droplet-specific measurements to better understand surfactant behavior in atmospheric particles.[8,19,20]

Aerosol photoelectron spectroscopy combined with velocity map imaging (VMI) is one of the few techniques capable of probing free droplet surfaces *in situ*. Photoelectron spectroscopy is inherently surface-sensitive and has been used to study surfactants at aqueous interfaces of microjets,[15,21] Langmuir troughs,[16] aerosol streams,[22] and droplet trains.[23] Applying photoelectron spectroscopy to aerosols is challenging as

[a] *Chemical Sciences Division, Lawrence Berkeley National Laboratory, Berkeley, CA 94720, USA. E-mail: krwilson@lbl.gov*
[b] *Department of Chemistry, University of California, Berkeley, Berkeley, CA 94720, USA*

plumes are typically dilute, leading to low sample volume and poor signal-to-noise ratios (SNR) in traditional photoelectron spectrometers.[22,23] To address this, Ahmed and co-workers[24] developed an aerosol photoelectron spectrometer incorporating VMI coupled to a synchrotron based tunable soft X-ray source.[25–28] This instrument captures all photoelectrons with kinetic energies below 60 eV, greatly improving the SNR compared to hemispherical analyzers, which only detect electrons over a narrow angular range. Since its development, the VMI-based aerosol photoelectron spectrometer has been used to study a variety of aqueous solutions and nanoparticles.[29–34] A persistent challenge remains, however, in accurately characterizing the physical state of aerosols and nanoparticles transmitted through vacuum to the point of detection, particularly their temperature and the concentration of aerosolized solutions after evaporation. Moreover, the structural characteristics of surfactant coatings have yet to be directly investigated in free aerosol particles.

Here aerosol velocity map imaging X-ray photoelectron spectroscopy (A-VMI-XPS) is used to investigate the surface adsorption and interfacial structure of a model atmospheric surfactant, *n*-octyl β-D-thioglucopyranoside (OTG), in submicron aerosols (20–250 nm radius). We characterize the aerosols at detection using mathematical models that quantify bulk phase depletion resulting from aerosolizing a macroscopic solution, as well as evaporative cooling as droplets enter the vacuum environment of the A-VMI-XPS instrument. Incorporating these corrections enables a direct comparison of OTG adsorption in aerosol droplets with that observed in bulk-phase studies. Furthermore, we demonstrate that A-VMI-XPS provides structural insights into surfactant layers on droplets through analysis of photoelectron angular distributions and secondary electron profiles, which reflect interfacial organization. The results of this work not only validate A-VMI-XPS as a robust technique for probing aerosol surfaces but also establish new approaches for connecting macroscopic surface studies to droplet-scale behavior, including in atmospheric contexts.

2. Methods

2.1. Experimental

Sodium chloride (>99%, Sigma-Aldrich) and *n*-octyl β-D-thioglucopyranoside (OTG, >95%, Thermofisher) were used without further purification. Eight OTG solutions with nominal concentrations of 0.600 mM, 0.750 mM, 0.850 mM, 1.00 mM, 1.25 mM, 2.50 mM, 5.00 mM, and 10.0 mM were made with ultrapure water (Milli-Q, 18.2 MΩ). Each solution also contained 0.500 M NaCl to ensure approximately constant water activity across all solutions.

Polydisperse nanodroplet aerosols were generated from the macroscopic bulk OTG solutions using an atomizer (TSI Model 3076). The size distributions of the aerosols produced by the atomizer were measured offline using a scanning mobility particle spectrometer (SMPS) consisting of a condensation particle counter (CPC 3025A, TSI Inc.) and a differential mobility analyzer (DMA 3071, TSI Inc.). Note that evaporation during SMPS measurements likely does not significantly affect the analysis presented here, see Section S11. Particle size distributions for aerosols generated from a 0.50 mM OTG solution and a 10 mM OTG solution are shown in Section S1. Both solutions result in aerosols with r = 20–250 nm. Since XPS is surface-sensitive, the particle size distribution is weighted by surface area, resulting in a surface-area weighted mean radius of 116 nm. During photoelectron spectroscopy experiments, aerosols traveled ~2 m in humidified air within copper tubing to reach the spectrometer inlet (Fig. 1), and we assume there is negligible evaporation during this time due to the high humidity.

XPS measurements were performed at the advanced light source (ALS) beamline 9.0.1 using an aerosol velocity map imaging X-ray photoelectron spectroscopy (A-VMI-XPS) instrument that has been described in detail previously.[24,35] A schematic is shown in Fig. 1. Aerosols enter the spectrometer *via* a 200 μm diameter nozzle and travel through an aerodynamic lens (ADL) comprised of a series of apertures designed to focus the droplets into a beam with a diameter ≤1 mm (see Section S2). At the inlet there is a significant pressure drop from atmosphere (760 Torr) to ~5 Torr, and two differential pumping regions immediately after the outlet of the ADL further reduce the pressure in the instrument to 10^{-6} Torr. We assume that the aerosols are in vacuum as soon as they pass the nozzle, and they travel a total of ~50 cm in vacuum before reaching the interaction region, where the particle beam interacts with the X-rays from the synchrotron. The stream of aerosols entering the spectrometer is constantly refreshed, avoiding artifacts due to X-ray damage. The photoelectrons generated when the aerosols are exposed to X-rays are directed toward the detector using VMI ion optics. The ion optics direct the generated photoelectrons toward the detector, which consists of microchannel plates, a phosphor screen, and a camera. Images are collected for 60 seconds with aerosols present, and a second set is collected without aerosols—using a particle filter—for gas phase background subtraction. The reconstructed velocity map images are obtained from the raw images using the pBASEX[36] algorithm. The scaling between radius in the reconstructed image and electron kinetic energy is calibrated using photoelectron spectra of gas-phase N_2 taken with 415–450 eV incident photons.

2.2. Modeling

The evaporative cooling of aerosols entering the spectrometer is calculated using the Hertz–Knudsen equation,[37,38]

$$\frac{1}{A}\frac{\mathrm{d}N}{\mathrm{d}t} = \frac{a_\mathrm{w} P_0}{\sqrt{2\pi m k_\mathrm{b} T}}, \quad (1)$$

where the evaporative molecular flux from the droplet surface, $\frac{1}{A}\frac{\mathrm{d}N}{\mathrm{d}t}$ (molecules cm^{-2} s^{-1}), is proportional to the vapor pressure, P_0, at the interface. In the present model, P_0 is parametrized with respect to temperature using the Arden Buck equation for pure water[39] leading to, for example, P_0 = 3.17 kPa at 298 K and $P_0 \sim 1 \times 10^{-3}$ kPA at 200 K. Eqn (1) also considers the mass m and temperature T of the evaporating species. This form has been used for evaporative cooling in

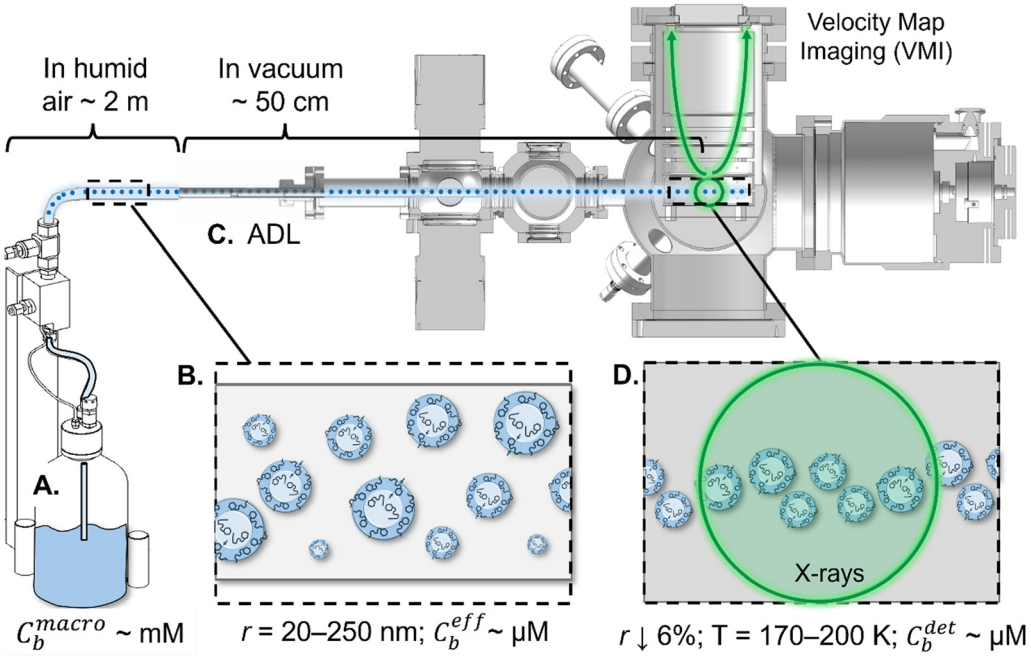

Fig. 1 Experiment schematic. (A) Bulk solutions with concentration C_b^{macro} are aerosolized by the nebulizer. (B) The plume consists of 20–250 nm radius aerosols. The increase in surface-area-to-volume ratio results in bulk depletion and effective concentration, C_b^{eff}. Aerosols are transferred ~2 m in humid air to the inlet of the spectrometer where they (C) pass through the aerodynamic lens (ADL), which collimates the plume. The aerosols undergo rapid evaporative cooling, and at the detection point (D), the radii have reduced by ~6%, increasing the concentration to C_b^{det}, and the temperature has dropped to 170–200 K. The VMI apparatus schematic is adapted with permission from Kostko *et al.*, *J. Chem. Phys.*, **147**, 013931. Copyright 2017 AIP Publishing.

liquid microjets, droplet trains, and within an ADL.[40–42] An additional term for water activity, a_w, is included to address potential solute effects. Given the low concentrations of OTG ($\leq$10 mM), we approximate the water activity as the mole fraction of water in the NaCl solution,

$$a_w = \frac{n_{H_2O}}{n_{H_2O} + n_{Na} + n_{Cl}}. \quad (2)$$

Mass loss at the interface is coupled with the aerosol temperature by,

$$\frac{dT}{dt} = -\frac{a_w P_0}{\sqrt{2\pi m k_b T}} \cdot \frac{\Delta H_{vap}}{C_p} \cdot \frac{3r^2}{\left(r^3 - (r-\delta)^3\right)\rho_{H_2O}}, \quad (3)$$

where ΔH_{vap} is the latent heat of vaporization for water, C_p is the heat capacity of water at constant pressure, and ρ_{H_2O} is the density of liquid water. The term $(r^3 - (r-\delta)^3)$ accounts for the volume of the interface, where we assume an interfacial thickness (δ) of 1 nm. For the aerosol size range investigated here ($r < 300$ nm), heat transfer across the entire droplet volume is rapid, and temperature gradients can be neglected. This is illustrated by estimating a timescale for heat diffusion across a particle with an upper-bound radius r = 300 nm. Using the thermal diffusivity of water at 0 °C of $D = 1.32 \times 10^{-3}$ cm^2 s^{-1}, we find an approximate timescale for heat transport across the particle, $\Delta t \sim r^2/D$ = 680 ns. Since the rate of evaporative cooling is on the μs–ms timescale, the effect of thermal gradients can be reasonably neglected for this size range. For micron-scale droplets, however, thermal gradients will form and could significantly impact evaporation rates. These dynamics can be resolved by introducing additional spatial compartments. Eqn (1)–(3) are solved simultaneously using numerical methods to compute aerosol size and temperature for evaporative lifetimes on the order of 1–10 ms.

3. Results and discussion

3.1. Accounting for aerosol effects

Aerosolized solutions of 0.60–10 mM *n*-octyl β-D-thioglucopyranoside (OTG) were studied in the A-VMI-XPS instrument as depicted in Fig. 1. Accurate interpretation of the photoelectron spectra requires understanding the final concentration in the aerosols at the detection point. For this, we consider the bulk concentration of the nebulized solution (C_b^{macro}), the effective bulk concentration in the aerosols after nebulization (C_b^{eff}), and the bulk concentration in the detected aerosols after evaporation in vacuum (C_b^{det}). Note that these concentrations are related to, but distinct from, the concentrations of adsorbed surfactant (C_{ads}) at each stage.

3.1.1. Bulk depletion. During aerosolization, there is a dramatic increase in the total surface area compared with the macroscopic sample (Fig. 1A and B). For example, if we completely aerosolize a cubic centimeter (1 cm × 1 cm × 1 cm) of solution forming aerosols with 100 nm radii, approximately 2×10^{14} aerosols will be formed. These aerosols will have a total surface area of 3×10^5 cm^2, much larger than the 1 cm^2 surface

area of the macroscopic solution. When aerosolizing solutions containing low concentrations of surface-active molecules, a larger portion of the molecules adsorb to the surface, but the substantial increase in surface area results in reduced concentrations in the bulk and at the surface. This effect, termed bulk depletion, can be calculated using previous models.[6,43] Here, we use the form derived by Alvarez *et al.*:[43]

$$\frac{C_b^{eff}}{C_b^{macro}} = \frac{1}{2}\left(1-\zeta-\frac{\zeta}{f}\right)+\frac{1}{2}\sqrt{\left(1-\zeta-\frac{\zeta}{f}\right)^2+4\frac{\zeta}{f}}, \quad (4)$$

where,

$$f = \frac{3K_L\Gamma_{max}}{r} \quad (5)$$

and

$$\zeta = \frac{3\Gamma_{max}}{C_b^{macro} r}. \quad (6)$$

K_L is the Langmuir adsorption equilibrium constant at 298 K, Γ_{max} is the maximum adsorbed concentration, and r is the mean radius. Macroscopic values of K_L and Γ_{max} for OTG on a 0.5 M NaCl solution are taken from Bain *et al.*[44] (K_{eq} = 5.9 ± 0.7 $m^3\ mol^{-1}$ and $\Gamma_{max} = 4.8\times10^{-6} \pm 0.2\times10^{-6}$ mol m^{-2}.) The XPS signal intensity is proportional to the concentration of species adsorbed to the interface rather than the number of particles. Representative size distributions are shown in Fig. 2A as particle count with respect to radius (closed circles) and total surface area with respect to radius (open triangles). We use the particles distribution expressed as total surface area (Fig. 2A open triangles) to determine the surface area weighted mean radius, 116 nm, which we use in Eqn (4)–(6). For comparison, the particle number (Fig. 2A closed circles) weighted mean radius, 59 nm, would underestimate the average size represented in photoelectron spectra.

Using eqn (4)–(6), we find that for the droplet sizes studied here (mean r = 116 nm), the effective bulk concentration is approximately two orders of magnitude lower than the macroscopic bulk concentration, or $C_b^{eff} \sim \frac{C_b^{macro}}{600}$, see Table 1. In other words, prior to aerosolization, the macroscopic bulk concentration is on the order of mM (Fig. 1A), but once aerosolized, partitioning to the surface reduces the bulk concentration in the aerosols to μM levels (Fig. 1B).

3.1.2. Evaporative cooling. Droplets with effective concentrations of C_b^{eff} enter the spectrometer through the aerodynamic lens (Fig. 1C) and undergo evaporative cooling, decreasing the droplet volume and increasing the bulk concentration by the point of detection (Fig. 1D). Once the aerosols enter, they travel ~50 cm before reaching the detection point. The speed of the aerosols is determined by the aerodynamic lens (ADL) design and can be calculated using the ADL calculator published by Wang and McMurry.[45] For the ADL used here, we calculate particle velocities of 102–236 m s^{-1} (see Section S2), resulting in 2–6 ms of evaporative cooling time prior to detection.

The method described in Section 2.2 is used to calculate changes in temperature and size for aerosols with a range of initial radii. A representative temperature profile for an aerosol with the average initial radius (r = 116 nm) is shown in Fig. 2B and final temperatures after 6 ms of evaporative cooling are shown in Fig. 2C. Importantly, evaporative cooling plateaus before 2 ms as indicated by the sharp drop in temperature shown in Fig. 2B. This results in a maximum radius reduction of approximately 6%, a minimal size change as demonstrated by the similar final radii at 2 ms and 6 ms, shown in Fig. 2A (open circles and red x's). Predicted temperatures at detection are between 170–200 K depending on the initial radius as shown in Fig. 2C. As discussed above, weighting the particle distribution by surface area is more appropriate for interpreting surface-selective photoelectron spectra, and we use the surface area weighted mean temperature, 188 K, for the remainder of this analysis. For reference, the

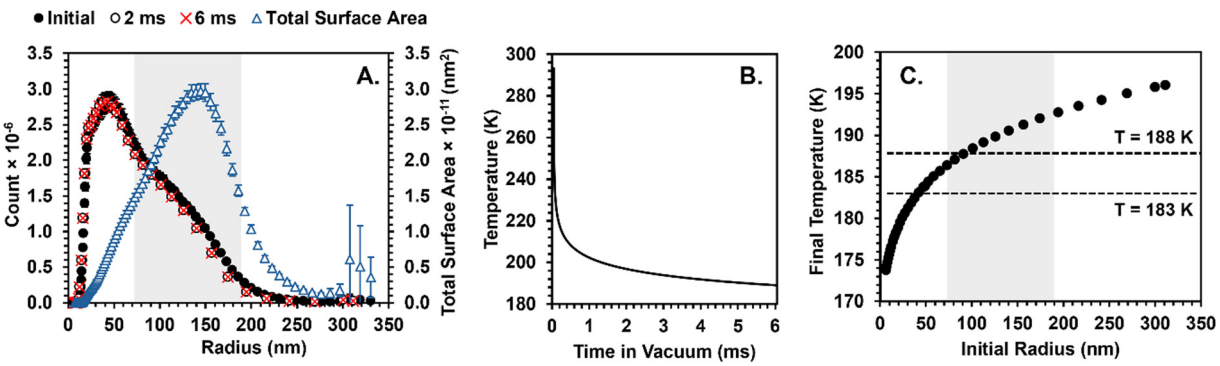

Fig. 2 (A) Particle count (black closed circles) and surface area (blue open triangles) with respect to droplet radius for OTG in 0.5 M aqueous NaCl. Particle count is plotted against the left y-axis and total surface area is plotted against the right y-axis. Note that particle count distributions were measured for both 0.5 mM OTG and 10 mM OTG solutions, but the distributions were indistinguishable (see Section S1). Error bars represent one standard deviation across three measurements of particle count. The predicted shifts in droplet radii after undergoing evaporative cooling for 2 ms (open circles) and 6 ms (red exes) are minimal. (B) Temperature profile for a 116 nm radius aerosol undergoing evaporative cooling in vacuum. (C) Predicted temperatures after 6 ms of evaporative cooling relative to initial particle radii. Horizontal dashed lines indicate the number averaged final temperature, 183 K, and the surface area averaged final temperature, 188 K. Shaded areas in (A) and (C) represent the particle radii, 70–190 nm, with total surface areas above the half maximum (*i.e.*, the most relevant sizes for analysis).

Table 1 Bulk concentration of OTG before nebulization (C_b^{macro}), after nebulization (C_b^{eff}), and after evaporation in vacuum (C_b^{det})

C_b^{macro} (mM)	C_b^{eff} (mM)	C_b^{eff} (μM)	C_b^{det} (μM)
10	1.5×10^{-2}	15	17.8
5.0	7.1×10^{-3}	7.1	8.6
2.5	3.5×10^{-3}	3.5	4.2
1.3	1.7×10^{-3}	1.7	2.1
1.0	1.4×10^{-3}	1.4	1.7
0.85	1.2×10^{-3}	1.2	1.4
0.75	1.0×10^{-3}	1.0	1.2
0.60	8.2×10^{-4}	0.82	1.0
0.50	6.8×10^{-4}	0.68	0.82

number weighted mean temperature, 183 K, would underpredict the average temperature represented by the photoelectron spectra.

Finally, we calculate the bulk concentration at detection, C_b^{det} by accounting for the volume decrease due to evaporation, shown in Table 1. The concentration at detection will be used for all further discussion.

3.2. X-ray photoelectron spectroscopy (XPS) results

Core level C (1s) XPS spectra of OTG aerosols with C_b^{det} = 0.82–17.8 μM (see Table 1 for corresponding macroscopic solution concentrations) were obtained using 310 eV incident photon energy. Note that the macroscopic solutions also contained 0.50 M NaCl to reduce the variability in aerosol sizes with changes in the macroscopic bulk OTG concentration. Spectra were collected as measured intensity with respect to electron kinetic energy (KE) and converted to intensity with respect to binding energies (BE), calculated by BE = 310 eV − KE. Binding energies are corrected by adding a constant offset such that the photoelectron peak assigned to the hydrocarbon tail is coincident with the nominal binding energy for a saturated hydrocarbon chain (285.0 eV).[46] Each spectrum was obtained in triplicate and representative spectra are shown as raw data in Fig. 3A and after baseline subtraction in Fig. 3B.

The raw data in Fig. 3A shows a significant contribution from secondary electrons, which are formed when primary electrons, including the photoelectrons discussed below, interact with the surrounding media. These interactions, or inelastic collisions, result in decreased kinetic energy and can cause secondary ionization, such as the ionization of the surrounding water. This contribution mainly appears at low kinetic energies that peak around 1 eV, but has a broad higher kinetic energy contribution, especially at higher OTG concentrations. Baselines, including contributions from secondary electrons, were subtracted by fitting cubic splines to the spectra, excluding the C 1s photoelectron peak region (BE = 282.6–288.6 eV). Sample baseline subtracted photoelectron data are shown in Fig. 3B. While this method over subtracts at the edges of the photoelectron peaks, this corresponds to a minimal reduction in overall intensity.

Two distinct photoelectron peaks are observed in Fig. 3B with BE = 285.0 eV and 286.6 eV, which are assigned to carbons in the hydrophobic tail and hydrophilic head, respectively (see Fig. 3B inset). A detailed description of this assignment is in Section S4. Baseline subtracted spectra are fit with two Gaussians to determine the signal intensity for each population of photoelectrons with respect to an increasing concentration of OTG in the aerosol bulk (C_b^{det}); representative fits are shown in Fig. 4A–G. See Section S5 for details regarding fitting procedure and parameters.

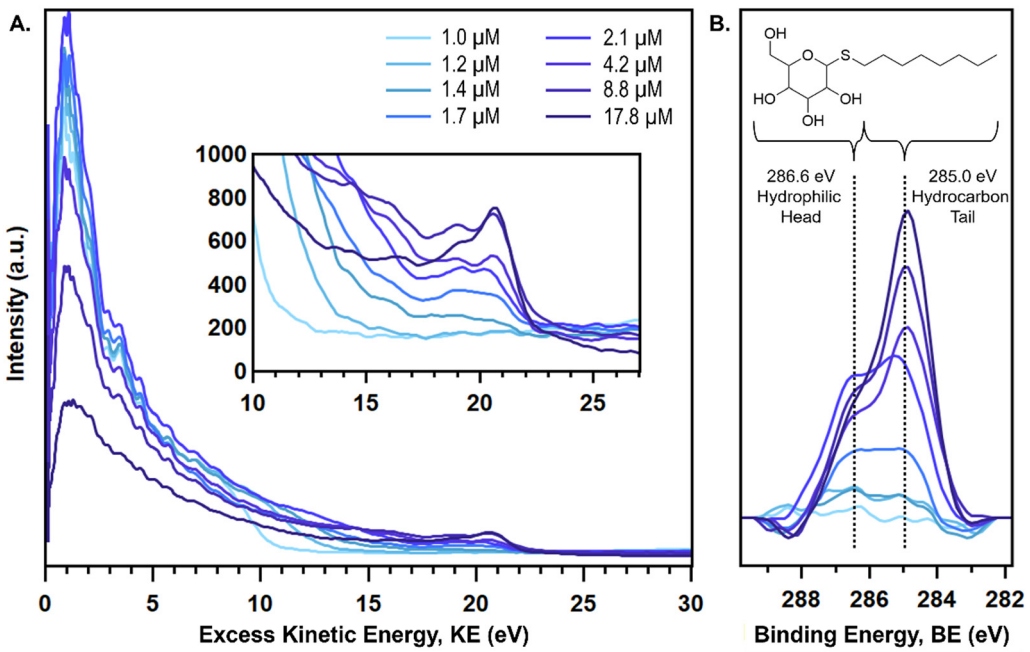

Fig. 3 Representative C 1s photoelectron spectra of aerosols with increasing OTG concentrations. (A) Raw data with respect to excess kinetic energy (KE) showing secondary electrons and photoelectrons. Inset focuses on photoelectrons. (B) Background subtracted photoelectron data with respect to corrected electron binding energy (BE) showing two populations of C 1s photoelectrons which can be assigned to the hydrocarbon tail (BE = 285.0 eV) and the hydrophilic head (BE = 286.6 eV). A second data set demonstrating repeatability can be seen in Section S3. (Inset) shows OTG structure.

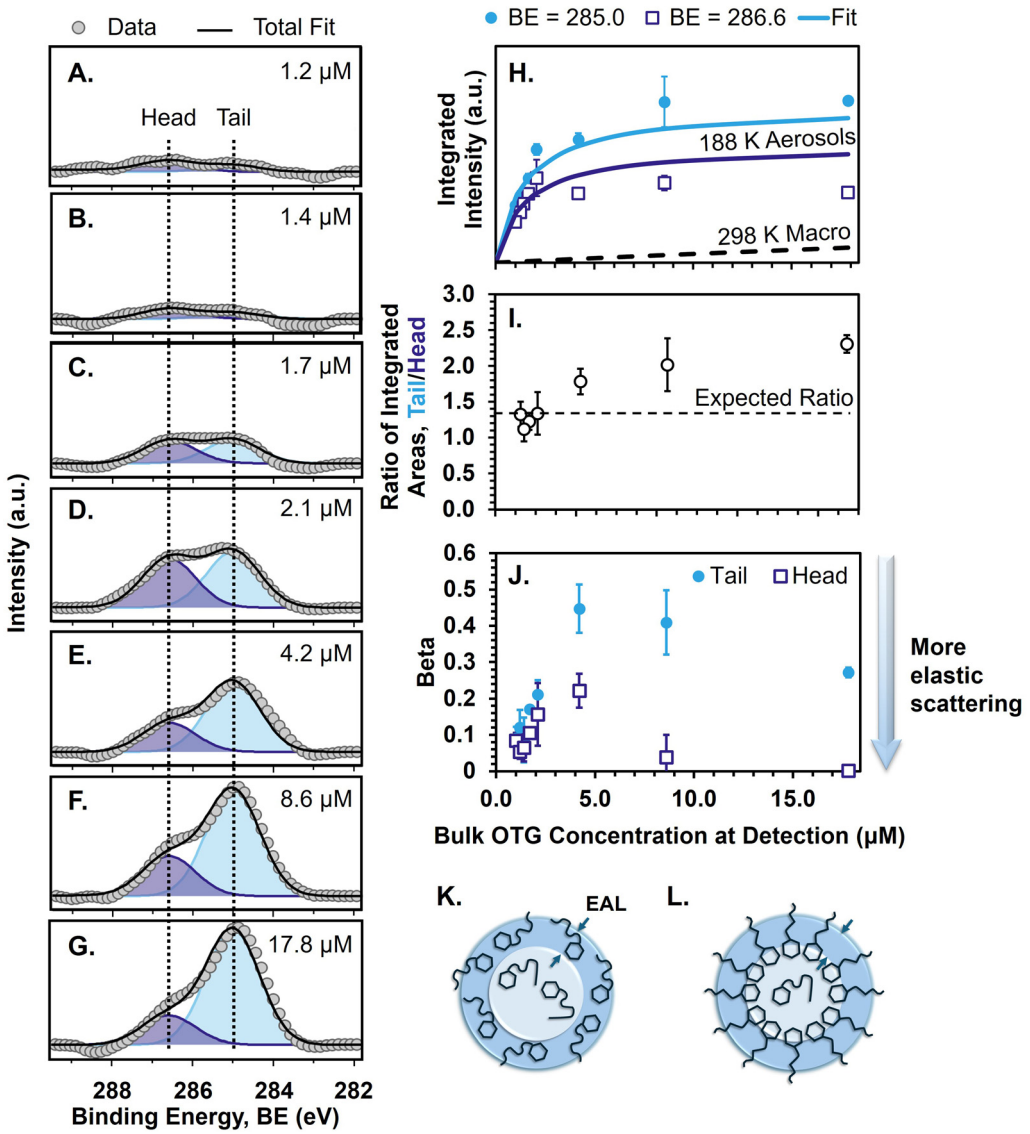

Fig. 4 Photoelectron analysis. (A)–(G) Representative fits to photoelectron spectra. Note that the representative 8.6 μM spectrum (F) is the average spectrum for clarity given the larger standard deviation in integrated intensities as shown in (H). (H) Integrated C 1s signal intensity with increasing bulk concentration of OTG at the detection point. Experimental intensities of photoelectrons emitted from the hydrocarbon tail (BE = 285.0 eV) are shown as closed circles and experimental intensities of photoelectrons emitted from the hydrophilic head (BE = 286.6 eV) are shown as open squares. Points are averages of fits to 2 or 3 spectra taken at each concentration. Error bars represent one standard deviation for each set. Lines represent the fit to the Langmuir adsorption model assuming T = 188 K (solid) and 298 K (dashed) as described in the main text. The integrated values from the second data set demonstrating repeatability can be seen in Section S3. (I) Ratios of the integrated peak areas. Ratios are calculated as the integrated area of the peak representing the hydrophobic tail divided by the integrated area of the peak representing the hydrophilic head. The expected ratio, 4 : 3, is indicated by the horizontal dashed line. (J) Beta asymmetry parameters representing the photoelectron angular distribution for electrons detached from tail carbons (closed circles) and head carbons (open squares). (K) and (L) Aqueous OTG droplet schematics (not to scale). (K) At low bulk concentrations the surface is not fully saturated, and all OTG molecules are likely disordered as shown. (L) At higher concentrations, a complete layer of OTG will be formed at the droplet surface, and the hydrocarbon tails likely extend beyond the condensed phase. The effective attenuation length (EAL) which represents the depth represented in the photoelectron spectra shown here, is indicated by the darker blue ring and arrows.

Integrated intensities for the 285.0 eV and 286.6 eV peaks are shown with respect to C_b^{det} in Fig. 4H for the primary data set and Section S3 for the secondary data set. The y-intercept of a linear fit to the first four data points was subtracted from all intensities to account for background signal. This ensures there is 0 intensity with 0 M OTG. Intensities increase with increasing C_b^{det} and plateau at $C_b^{eff} > 2$ μM, consistent with Langmuir adsorption behavior.

We also examine the relative intensities of the two C 1s peaks, which should reflect the ratio of the number of carbons that each peak represents. Here, the 285.0 eV peak consists of photoelectrons ejected from the 8 carbons in the hydrophobic tail and the 286.6 eV peak consists of photoelectrons ejected from the 6 carbons in the hydrophilic head (Fig. 3B inset), resulting in a tail to head intensity ratio of 4 : 3. This expected ratio is compared to measured intensity ratios in Fig. 4I.

Interestingly, experimental ratios are consistent with the expected ratio for $C_b^{det} < 3$ μM, but increase beyond 4 : 3 at [OTG] > 3 μM where adsorption appears to plateau. This is discussed further in Section 3.4.

3.3. Adsorption behavior

As previously discussed, direct interrogation of surfactant adsorption at droplet interfaces presents significant challenges. Here, we exploit the surface-selectivity of A-VMI-XPS and quantitatively probe OTG adsorption at the surface of aerosols by fitting the integrated peak areas with a Langmuir adsorption isotherm,

$$\theta = \frac{\Gamma}{\Gamma_{max}} = \frac{K_L C_b^{det}}{1 + K_L C_b^{det}}, \quad (7)$$

where θ is the surface coverage expressed as a unitless value between 0 (no coverage) and 1 (full coverage), K_L is the Langmuir adsorption equilibrium constant in m^3 mol^{-1}, and C_b^{det} is the bulk concentration at detection. As shown in eqn (7), θ is typically expressed as the surface excess Γ divided by the maximum surface excess Γ_{max}. Here, we assume that Γ_{max} would lead to a maximum observable photoelectron peak intensity, I_{max}, and instead express θ as a ratio of intensities, $\frac{I}{I_{max}}$.

Eqn (7) was fit to both C 1s peaks simultaneously with I_{max} and K_L as the adjustable parameters. Note that while K_L represents Langmuir adsorption for the entire molecule, the intensity of the photoelectron signal (I and I_{max}) has a linear relationship with the number of atoms that contribute to that signal. To account for the different number of atoms contributing to the tail (8 carbons) and head photoelectron peaks (6 carbons), we use I_{max} for the tail peak and $0.75 \times I_{max}$ for the head peak. A Langmuir equilibrium constant, K_L, of 700 m^3 mol^{-1} is obtained from the fit shown in Fig. 4H. Fitting eqn (7) to the second set of data shown in Section S3 resulted in a calculated experimental equilibrium constant of 900 m^3 mol^{-1}, which shows reasonable agreement given experimental uncertainties and fit sensitivities, which are discussed further below. Notably, the experimental peak intensities shown in Fig. 4H diverge from the fit intensities after the onset of surface saturation around 2 μM—especially for the photoelectron peak corresponding to the hydrophilic head group—suggesting that the structure of the adsorbed layer affects the observed Langmuir behavior (discussed further in Section 3.4).

Few studies have directly compared surface adsorption in droplets to macroscale adsorption.[6,9,44] Here, we compare the equilibrium constants determined for supercooled nanoscale droplets to equilibrium constants determined for room temperature macroscale flat surfaces, using the thermodynamic relationship:

$$\frac{K_L}{\gamma} C^0 = \exp\left(\frac{-\Delta G_{ads}}{RT}\right), \quad (8)$$

where ΔG_{ads} is the Gibbs free energy of adsorption, R is the universal gas constant, T is temperature, γ is the activity coefficient, and C^0 is the concentration of the standard reference solution, 10^3 mol m^{-3}.[47] Note that there is extensive debate in the literature regarding the correct method for resolving unit discrepancies when converting between Langmuir equilibrium constants and Gibbs free energies of adsorption.[47,48] Here, we use the formulation in eqn (8) as it can be directly derived from the Langmuir definition of equilibrium.[47] Rearranging to solve for ΔG_{ads} and assuming that ΔG_{ads} is the same in the supercooled nanoscale droplets and room temperature macroscale flat surfaces, we can compute K_L at room temperature:

$$K_L^{298K} = \frac{\gamma}{C^0} \exp\left[\frac{T}{298\ K} \ln\left(K_L \frac{C^0}{\gamma}\right)\right], \quad (9)$$

where T = 188 K, the surface area-weighted average temperature determined by the evaporative cooling model discussed in Section 3.1.2, and γ is the activity coefficient. There is some evidence that the activity coefficient of supercooled water may be less than 1,[49,50] but there are no direct measurements of water activity at the temperatures and pressures studied here. Additionally, a lower activity coefficient does not significantly affect the calculated K_{eq}^{298K}, see Section S10. We thus use the activity coefficient at room temperature, γ = 1, for consistency with macroscopic measurements.

We find K_{eq}^{298K} values of 4.9 m^3 mol^{-1} from the data shown in Fig. 4H and 5.7 m^3 mol^{-1} from the data in Section S3. These values are consistent with macroscopic surface tension measurements for 0.5 M NaCl solutions containing varying concentrations of OTG.[9,44] A Langmuir fit to the literature surface tension data[9] yielded K_L = 5.9 ± 0.7 m^3 mol^{-1}, though the reported uncertainty only reflects the fit error, not the error that would arise from uncertainty in Γ_{max} discussed below.[44] In practice, Langmuir equilibrium constants can span several orders of magnitude depending on the surfactant's surface activity—for example, $K_L > 500$ m^3 mol^{-1} for Tween20 and $K_L > 35\,000$ m^3 mol^{-1} for C14E6, a linear poly(oxyethylene) alkyl ether.[44] Additionally, changes in K_L within the same order of magnitude still adequately represent the experimental data from Bain, *et al.*[9] when the maximum surface concentration, Γ_{max}, is allowed to vary, as shown in Section S6. Varying Γ_{max} between 4×10^{-6} mol m^{-2} and 6×10^{-6} mol m^{-2} adequately recreates the Bain, *et al.*[9] macroscopic surface tension data. These values correspond to molecular footprints between 28 $Å^2$ per molec. and 42 $Å^2$ per molec., which are both physically realistic. The K_L values reported here (4.9 m^3 mol^{-1} and 5.7 m^3 mol^{-1}) and the mean value reported in the literature[44] (5.9 m^3 mol^{-1}) are in reasonable agreement considering the uncertainties of both experiments. This agreement between nano- and macroscale Langmuir equilibrium constants required quantitatively accounting for the substantial bulk depletion and lowered temperatures in the aerosols studied here.

Predicted intensities based on the room-temperature Langmuir equilibrium constant (4.9 m^3 mol^{-1}) are shown in Fig. 4H (dashed line), representing expected surfactant adsorption assuming only bulk depletion. The substantial underprediction of intensity aligns with the two-order-of-magnitude decrease in the equilibrium constant—from 700 m^3 mol^{-1} at 188 K to 4.9 m^3 mol^{-1} at room temperature. Notably, atmospheric aerosols can encounter temperatures as low as −60 °C (213 K), particularly

in the upper troposphere and stratosphere, indicating that surfactant adsorption in natural environments may be significantly greater than what is typically observed under room-temperature laboratory conditions.

3.4. Surfactant coating structure

The A-VMI-XPS results also provide insight into the structure of the surfactant coating, offering additional context for atmospheric aerosol behavior and helping to explain the previously noted deviations in photoelectron peak intensities. At high surfactant concentrations, the photoelectron peak ratios diverge from the expected values (Fig. 4I), and the headgroup photoelectron intensities deviate from those predicted by the Langmuir fit (Fig. 4H). We offer a physical picture for the expected structure of OTG on droplet surfaces to explain these deviations. The structure of organic monolayers on flat aqueous surfaces has been well characterized in the literature, and amphiphilic molecules like OTG are expected to align with their hydrophilic head groups pointing towards the water and their hydrophobic tails pointed away. At low bulk concentrations, when surface coverage is low, molecules disperse, and the hydrophobic tails adopt more disordered configurations (Fig. 4K). As the bulk concentration increases, more molecules adsorb to the air–water interface, eventually reaching full surface coverage and forcing the hydrophobic tails into more ordered configurations, which may extend beyond the condensed phase (Fig. 4L).

In photoelectron spectroscopy, the photoelectron peak intensities are related to the likelihood that an electron can reach the detector, which is often defined by the electron's effective attenuation length (EAL). The EAL accounts for electron loss due to scattering, and most of the detected electrons can be assumed to originate from within this depth. In the dilute case (Fig. 4K), photoelectrons emitted from the hydrophilic head group and hydrophobic tail likely experience similar scattering and have similar EALs, resulting in experimental relative intensities that are consistent with the expected value of 1.33 (4 : 3). As the monolayer becomes more packed, however, the hydrocarbon tails extend into the vacuum, decreasing scattering and increasing the EAL for photoelectrons ejected from the tail and increasing the relative number of tail photoelectrons that reach the detector. Meanwhile, the photoelectrons ejected from the hydrophilic head group would experience the same EAL as in the dilute monolayer case, resulting in a plateau in the detected head photoelectron intensity above 3 μM as observed in Fig. 4H (open squares). Taken together, this would cause the ratio of tail to head photoelectron intensities to increase above 1.33 as observed for $C_b^{det} > 3$ μM (Fig. 4I).

To further explore this hypothesis, we examine the photoelectron angular distribution, which can be used as a qualitative indicator of elastic scattering.[15,51] Briefly, the electron emission angles are expected to be anisotropic due to the interaction with the p-polarized incident X-ray radiation. This anisotropy is quantified by β, calculated from the angle-dependent intensity,

$$I(\theta) = 1 + \frac{\beta}{2}\left(3\cos^2\theta - 1\right). \quad (10)$$

A 1s electron emitted from a single atom in the gas phase with high kinetic energy will have increased intensity along the incident radiation's polarization axis and decreased intensity perpendicular to the polarization axis resulting in $\beta = 2$. However, photoelectron emission angles become more isotropic for photoelectrons that scatter from other molecules or photoelectrons with lower kinetic energies, which allow for greater interaction with molecular orbitals. At $\beta = 0$, the angular distribution is fully isotropic. See Section S7 for further details about fitting β to the data presented here.

The anisotropy parameters for both head and tail photoelectron populations are shown in Fig. 4J. As the bulk concentration increases below the surface saturation point (3 μM), β for both populations increases, which can be attributed to less scattering as more OTG molecules are pushed to the interface. The slight differences between the β values for each population at $C_b^{det} < 3$ μM likely arise from the different kinetic energies, but the differences become much larger at $C_b^{det} > 3$ μM. This can be attributed to a shift in molecular morphology such as that shown in Fig. 4K–L. OTG molecular disorder at low bulk concentrations would result in head and tail photoelectron emissions at similar depths from the interface, while the straightened hydrocarbon chains at higher bulk concentrations would result in a lower effective depth for the tail photoelectrons and a higher effective depth for the head photoelectrons. Previous studies[52,53] on amphiphilic organic molecules have shown that the lower β values of hydrophilic head photoelectrons can be associated with the head group being submerged further from the interface, and the higher β values of hydrophobic tail photoelectrons can be associated with the tail being closer to the air–water interface. Thus, the separation between β values for $C_b^{det} > 3$ μM shown in Fig. 4J is consistent with the ordered monolayer structure depicted in Fig. 4L.

The subsequent decrease in β values for both head- and tail-related photoelectrons with further increases in bulk concentration likely occurs due to increased packing of the surface layer beyond full surface coverage, possibly forming a concentrated surfactant shell around the droplet surface. This is supported by an analysis of the secondary electrons; the population of secondary electrons (shown in Fig. 3A as the rise in intensity at low KE) can be fit by the Henke, *et al.*[54] model, providing a measure of the barrier to electron escape from the particle. The distribution of secondary electrons (SEs) can be qualitatively fit with the relationship $I(\mathrm{KE}) = k\frac{\mathrm{KE}}{(\mathrm{KE} + E_A)^3}$, where I is the kinetic energy-dependent intensity, k is a unitless fitting factor, KE is the electron kinetic energy, and E_A is the electron affinity energy with units of eV.[24,54] In this context, k represents the total intensity of detected SEs and E_A represents the barrier to escape. See Section S8 for representative fits. In Fig. 5A, we see that there are more SEs detected with increasing concentration up to the surface saturation point (3 μM). Given

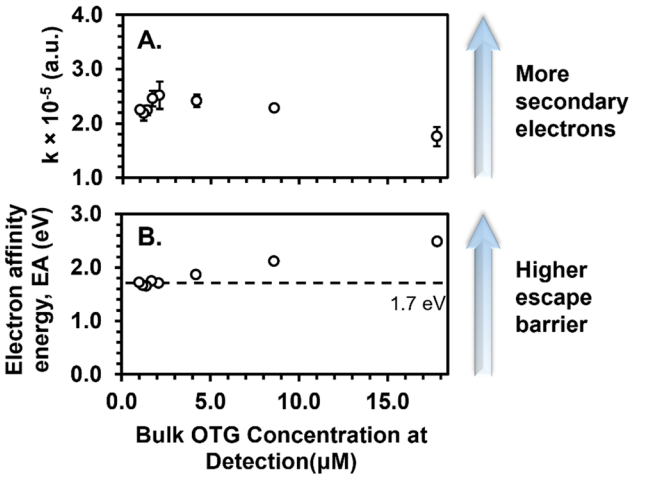

Fig. 5 Secondary electron fit parameters k (panel A) and electron affinity energy (E_A, panel B).

the constant electron affinity E_A = 1.7 eV in this concentration range, the increased signal directly correlates with more SE formation, consistent with the enhanced photoelectron intensity shown in Fig. 4H. With increasing concentration beyond 3 μM, however, the SE signal decreases and the electron affinity energy increases, suggesting a larger barrier that prevents SE escape for detection. Kostko, *et al.*[24] found that squalene nanoparticles had an E_A of 4.4 eV, suggesting that an organic layer would indeed have a higher SE escape barrier. Thus, the increasing value for E_A seen in Fig. 5B supports the hypothesis that a concentrated surfactant layer forms around the droplet.

Taken together, the divergence between predicted and measured photoelectron peak intensities (Fig. 4H), increasing photoelectron peak intensity ratios (Fig. 4I), decreasing β values (Fig. 4J), and increasing electron affinity barriers (Fig. 5B)—all at concentrations above 3 μM—present strong evidence for a concentrated surfactant layer at the surface of the aerosols. This is particularly striking when we consider that very little surfactant would be at the droplet surface at room temperature given the bulk depletion that occurs during aerosolization.

4. Conclusions

Accurate quantification of the impact of surfactants on atmospheric processes requires surface-sensitive measurements in droplets. Aerosol velocity map imaging X-ray photoelectron spectroscopy (A-VMI-XPS) provides direct probing of droplet surfaces, offering advantages over flat or cylindrical liquid microjet setups that only model them. However, a key barrier to broader adoption has been the uncertainty about aerosol behavior in vacuum. Here, we studied surfactant adsorption and structure in sub-micron aerosols (10–250 nm radius) produced from solutions with varying concentrations of OTG, a model atmospheric surfactant. Modeling predicted bulk concentration reduction by a factor of 600 during aerosolization, minimal evaporation (<6% by radius), and rapid cooling to an average temperature of 188 K in the A-VMI-XPS instrument. Kostko *et al.*[24] suggested droplets in the spectrometer may exist in a supercooled or mixed-phase state. While further work is ongoing to distinguish between these two possibilities, the agreement between the Langmuir isotherm and the experimental data shown here may suggest that at least the surface of the aerosol remains liquid.

We fit concentration-dependent photoelectron intensities—corrected for bulk depletion—to a modified Langmuir equation, demonstrating significant surface adsorption in the supercooled 188 K aerosols (K_L = 700 m^3 mol^{-1} and 900 m^3 mol^{-1} for the two data sets). We use eqn (9) to calculate equivalent room temperature Langmuir adsorption constants, K_L^{298K} = 4.9 m^3 mol^{-1} and 5.7 m^3 mol^{-1}, a remarkable 2 orders-of-magnitude decrease in adsorption with the increased temperature. Additionally, the calculated values of K_L^{298K} show reasonable agreement with the mean literature value of 5.9 m^3 mol^{-1}.[44] This establishes that Langmuir adsorption constants in sub-micron droplets can be linked to those from flat macroscopic surfaces by considering bulk depletion and temperature effects on adsorption.

Despite its lower kinetic energy resolution compared to hemispherical analyzers, A-VMI-XPS uniquely enables structural studies of surfactants on droplet surfaces. VMI captures all emitted electrons with kinetic energies below 60 eV, allowing simultaneous detection of photoelectron and secondary electron populations, including direct measurement of photoelectron angular distributions. The measured changes in relative photoelectron intensities, decreased photoelectron anisotropy (β), reduced secondary electron signals, and increased escape barriers all indicate that aerosols develop a concentrated surfactant surface layer at high bulk OTG concentrations. Differences in head and tail photoelectron anisotropy at these concentrations indicate a more ordered surfactant layer. Many studies have examined the structure of surfactants at flat water surfaces or their influence on the physicochemical properties of droplets. However, few have directly probed the surfactant structure on free droplets with surface-specificity.[19,55,56] To our knowledge, this is one of the first *in situ* investigations of the surfactant layer on droplets—and the first to use XPS to analyze surfactant structure on aqueous droplets.

It is noteworthy that the temperature of the aerosols in the A-VMI-XPS instrument (188 K) approaches the temperature of atmospheric aerosols, which may be as low as −60 °C (213 K). This similarity in temperatures suggests that atmospheric aerosols, particularly those in the upper troposphere and stratosphere, likely also exhibit the significant increase in adsorption demonstrated here. Consequently, the use of room-temperature adsorption equilibrium constants in atmospheric models could substantially underpredict surfactant adsorption—potentially by orders of magnitude. Additionally, the contactless environment in the A-VMI-XPS instrument may facilitate the study of supercooled aerosols, overcoming limitations in conventional lab setups where similar studies are challenging. Analogous investigations of nebulized solutions, using the A-VMI-XPS instrument or a similar contactless and temperature-dependent technique, can serve as a necessary complement to those performed in the room temperature laboratory environment. Aerosol photoelectron spectroscopy

offers a valuable method to study gas–liquid interfaces, providing detailed insights into microdroplet chemistry and surfactant behavior with implications for atmospheric processes such as cloud formation.

Conflicts of interest

There are no conflicts of interest to declare.

Data availability

The data for this manuscript are included in the SI.

Additional information is provided regarding particle size distributions, the aerodynamic lens, repeat XPS spectra, photoelectron peak assignments, photoelectron peak fitting, Langmuir fits to macroscopic surface tension data, beta parameter fitting, secondary electron fitting, sensitivity to the activity coefficient for supercooled water, and the impact of evaporation during particle size measurements. See DOI: **https://doi.org/10.1039/d5cp02126j**

Acknowledgements

The experimental measurements, modeling and XPS analysis were supported by the Condensed Phase and Interfacial Molecular Science Program (CPIMS), in the Chemical Sciences Geosciences and Biosciences Division of the Office of Basic Energy Sciences of the U.S. Department of Energy under contract No. DE-AC02-05CH11231. Particle size measurements and the analysis of the secondary electron signals were supported by the Gas Phase Chemical Physics Program (GPCP) in the Chemical Sciences Geosciences and Biosciences Division of the Office of Basic Energy Sciences of the U.S. Department of Energy under contract No. DE-AC02-05CH11231. The Advanced Light Source (ALS) is supported under the same contract. MMF acknowledges support from the Arnold and Mabel Beckman Foundation through the Arnold O. Beckman Postdoctoral Fellowship. AMD acknowledges support from the University of Michigan during revisions. We thank Prof. Alison Bain for the advice in working with OTG.

References

1 P. Arias, N. Bellouin, E. Coppola, R. Jones, G. Krinner, J. Marotzke, V. Naik, M. Palmer, G.-K. Plattner and J. Rogelj, *Climate Change 2021: The Physical Science Basis. Contribution of Working Group I to the Sixth Assessment Report of the Intergovernmental Panel on Climate Change; Technical Summary*, Cambridge University Press, Cambridge, UK, 2021.

2 C. R. Ruehl, J. F. Davies and K. R. Wilson, An Interfacial Mechanism for Cloud Droplet Formation on Organic Aerosols, *Science*, 2016, **351**(6280), 1447–1450, DOI: **10.1126/science.aad4889**.

3 J. F. Davies, A. Zuend and K. R. Wilson, Technical Note: The Role of Evolving Surface Tension in the Formation of Cloud Droplets, *Atmos. Chem. Phys.*, 2019, **19**(5), 2933–2946, DOI: **10.5194/acp-19-2933-2019**.

4 R. Sorjamaa, B. Svenningsson, T. Raatikainen, S. Henning, M. Bilde and A. Laaksonen, The Role of Surfactants in Köhler Theory Reconsidered, *Atmos. Chem. Phys.*, 2004, **4**, 2107–2117, DOI: **10.5194/acp-4-2107-2004**.

5 N. Sareen, A. N. Schwier, T. L. Lathem, A. Nenes and V. F. McNeill, Surfactants from the Gas Phase May Promote Cloud Droplet Formation, *Proc. Natl. Acad. Sci. U. S. A.*, 2013, **110**(8), 2723–2728, DOI: **10.1073/pnas.1204838110**.

6 K. R. Wilson and A. M. Prophet, Chemical Kinetics in Microdroplets, *Annu. Rev. Phys. Chem.*, 2024, **75**(1), 185–208, DOI: **10.1146/annurev-physchem-052623-120718**.

7 A. Prophet, D. Limmer and K. Wilson, *Surfactant Control of Interfacial Reaction Rates in Aqueous Microdroplets*, *ChemRxiv*, 2024, preprint, chemrxiv-2024-mj9gg, DOI: **10.26434/chemrxiv-2024-mj9gg**. This content is a preprint and has not been peer-reviewed.

8 M. El Haber, V. Gérard, J. Kleinheins, C. Ferronato and B. Nozière, Measuring the Surface Tension of Atmospheric Particles and Relevant Mixtures to Better Understand Key Atmospheric Processes, *Chem. Rev.*, 2024, **124**(19), 10924–10963, DOI: **10.1021/acs.chemrev.4c00173**.

9 A. Bain, K. Ghosh, N. L. Prisle and B. R. Bzdek, Surface-Area-to-Volume Ratio Determines Surface Tensions in Microscopic, Surfactant-Containing Droplets, *ACS Central Sci.*, 2023, **9**(11), 2076–2083, DOI: **10.1021/acscentsci.3c00998**.

10 M. I. Jacobs, M. N. Johnston and S. Mahmud, Exploring How the Surface-Area-to-Volume Ratio Influences the Partitioning of Surfactants to the Air-Water Interface in Levitated Microdroplets, *J. Phys. Chem. A*, 2024, **128**(46), 9986–9997, DOI: **10.1021/acs.jpca.4c06210**.

11 M. G. V. de Vasquez, K. A. Carter-Fenk, L. M. McCaslin, E. E. Beasley, J. B. Clark and H. C. Allen, Hydration and Hydrogen Bond Order of Octadecanoic Acid and Octadecanol Films on Water at 21 and 1 °C, *J. Phys. Chem. A*, 2021, **125**(46), 10065–10078, DOI: **10.1021/acs.jpca.1c06101**.

12 A. E. Smith, K. M. Oyala, G. H. Campolo, B. E. Rugeley, T. A. Mose, D. L. Talley, A. M. Deal, C. B. Cooley and R. J. Rapf, Infrared Reflection-Absorption Spectroscopy of α-Keto Acids at the Air-Water Interface: Effects of Chain Length and Headgroup on Environmentally Relevant Surfactant Films, *J. Phys. Chem. A*, 2023, **127**(18), 4137–4151, DOI: **10.1021/acs.jpca.3c01266**.

13 L. B. Dreier, M. Bonn and E. H. G. Backus, Hydration and Orientation of Carbonyl Groups in Oppositely Charged Lipid Monolayers on Water, *J. Phys. Chem. B*, 2019, **123**(5), 1085–1089, DOI: **10.1021/acs.jpcb.8b12297**.

14 C. C. Yu, T. Seki, K. Y. Chiang, Y. K. Wang, M. Bonn and Y. Nagata, Depth-profiling Alkyl Chain Order in Unsaturated Lipid Monolayers on Water, *J. Chem. Phys.*, 2024, **160**(11), 114902, DOI: **10.1063/5.0190519**.

15 R. Dupuy, J. Filser, C. Richter, R. Seidel, F. Trinter, T. Buttersack, C. Nicolas, J. Bozek, U. Hergenhahn and

H. Oberhofer, *et al.*, Photoelectron Angular Distributions as Sensitive Probes of Surfactant Layer Structure at the Liquid-Vapor Interface, *Phys. Chem. Chem. Phys.*, 2022, **24**(8), 4796–4808, DOI: 10.1039/d1cp05621b.

16 H. Hoek, T. Gerber, C. Richter, R. Dupuy, R. J. Rapf, H. Oertel, T. Buttersack, L. Trotochaud, O. Karslioglu and D. Goodacre, *et al.*, Compression of a Stearic Acid Surfactant Layer on Water Investigated by Ambient Pressure X-ray Photoelectron Spectroscopy, *J. Phys. Chem. B*, 2024, **128**(15), 3755–3763, DOI: 10.1021/acs.jpcb.4c00451.

17 M. Irwin, N. Good, J. Crosier, T. W. Choularton and G. McFiggans, Reconciliation of Measurements of Hygroscopic Growth and Critical Supersaturation of Aerosol Particles in Central Germany, *Atmos. Chem. Phys.*, 2010, **10**(23), 11737–11752, DOI: 10.5194/acp-10-11737-2010.

18 J. Heitland, J. C. Lee, L. R. Ban, G. L. Abma, W. G. Fortune, H. H. Fielding, B. L. Yoder and R. Signorell, Valence Electronic Structure of Interfacial Phenol in Water Droplets, *J. Phys. Chem. A*, 2024, **128**(35), 7396–7406, DOI: 10.1021/acs.jpca.4c04269.

19 T. Lei, M. F. Ge and W. G. Wang, Analysis of Atmospheric Particles: From the Bulk to the Interface, *Anal. Chem.*, 2025, **97**(18), 9554–9568, DOI: 10.1021/acs.analchem.4c06795.

20 A. P. Ault and J. L. Axson, Atmospheric Aerosol Chemistry: Spectroscopic and Microscopic Advances, *Anal. Chem.*, 2017, **89**(1), 430–452, DOI: 10.1021/acs.analchem.6b04670.

21 N. L. Prisle, Surfaces of Atmospheric Droplet Models Probed with Synchrotron XPS on a Liquid Microjet, *Acc. Chem. Res.*, 2023, **57**(2), 177–187, DOI: 10.1021/acs.accounts.3c00201.

22 E. R. Mysak, D. E. Starr, K. R. Wilson and H. Bluhm, Note: A Combined Aerodynamic Lens/Ambient Pressure x-ray Photoelectron Spectroscopy Experiment for the On-Stream Investigation of AerosolSurfaces, *Rev. Sci. Instrum.*, 2010, **81**, 016106, DOI: 10.1063/1.3276714.

23 D. E. Starr, E. K. Wong, D. R. Worsnop, K. R. Wilson and H. Bluhm, A Combined Droplet Train and Ambient Pressure Photoemission Spectrometer for the Investigation of Liquid/Vapor Interfaces, *Phys. Chem. Chem. Phys.*, 2008, **10**(21), 3093–3098, DOI: 10.1039/b800717a.

24 O. Kostko, B. Xu, M. Jacobs and M. Ahmed, Soft X-ray spectroscopy of nanoparticles by velocity map imaging, *J. Chem. Phys.*, 2017, **147**, 013931, DOI: 10.1063/1.4982822.

25 K. R. Wilson, H. Bluhm and M. Ahmed, 15 Aerosol Photoemission, in *Fundamentals and Applications in Aerosol Spectroscopy*, 2010, p. 367.

26 K. R. Wilson, D. S. Peterka, M. Jimenez-Cruz, S. R. Leone and M. Ahmed, VUV Photoelectron Imaging of Biological Nanoparticles: Ionization Energy Determination of Nanophase Glycine and Phenylalanine-Glycine-Glycine, *Phys. Chem. Chem. Phys.*, 2006, **8**(16), 1884–1890, DOI: 10.1039/b517487b.

27 K. R. Wilson, S. L. Zou, J. N. Shu, E. Ruhl, S. R. Leone, G. C. Schatz and M. Ahmed, Size-dependent Angular Distributions of Low-energy Photoelectrons Emitted from NaCl Nanoparticles, *Nano Lett.*, 2007, **7**(7), 2014–2019, DOI: 10.1021/nl070834g.

28 J. N. Shu, K. R. Wilson, M. Ahmed and S. R. Leone, Coupling a Versatile Aerosol Apparatus to a Synchrotron: Vacuum Ultraviolet Light Scattering, Photoelectron Imaging, and Fragment Free Mass Spectrometry, *Rev. Sci. Instrum.*, 2006, **77**(4), 043106, DOI: 10.1063/1.2194474.

29 C. Weeraratna, C. Amarasinghe, W. C. Lu and M. Ahmed, A Direct Probe of the Hydrogen Bond Network in Aqueous Glycerol Aerosols, *J. Phys. Chem. Lett.*, 2021, **12**(23), 5503–5511, DOI: 10.1021/acs.jpclett.1c01383.

30 P. Kim, C. Weeraratna, S. Nemsák, N. Dias, A. K. Lemmens, K. R. Wilson and M. Ahmed, Interfacial Nanostructure and Hydrogen Bond Networks of Choline Chloride and Glycerol Mixtures Probed with X-ray and Vibrational Spectroscopies, *J. Phys. Chem. Lett.*, 2024, **15**(11), 3002–3010, DOI: 10.1021/acs.jpclett.4c00052.

31 C. Weeraratna, X. C. Tang, O. Kostko, V. H. Rapp, L. A. Gundel, H. Destaillats and M. Ahmed, Fraction of Free-Base Nicotine in Simulated Vaping Aerosol Particles Determined by X-ray Spectroscopies, *J. Phys. Chem. Lett.*, 2023, **14**(5), 1279–1287, DOI: 10.1021/acs.jpclett.2c03748.

32 P. C. Lin, Z. H. Wu, M. S. Chen, Y. L. Li, W. R. Chen, T. P. Huang, Y. Y. Lee and C. C. Wang, Interfacial Solvation and Surface pH of Phenol and Dihydroxybenzene Aqueous Nanoaerosols Unveiled by Aerosol VUV Photoelectron Spectroscopy, *J. Phys. Chem. B*, 2017, **121**(5), 1054–1067, DOI: 10.1021/acs.jpcb.6b10201.

33 R. Signorell, M. Goldmann, B. L. Yoder, A. Bodi, E. Chasovskikh, L. Lang and D. Luckhaus, Nanofocusing, Shadowing, and Electron Mean Free path in the Photoemission from Aerosol Droplets, *Chem. Phys. Lett.*, 2016, **658**, 1–6, DOI: 10.1016/j.cplett.2016.05.046.

34 E. Antonsson, F. Gerke, B. Langer, C. Goroncy, T. Dresch, T. Leisner, C. Graf and E. Rühl, Inelastic mean-free path and mean escape depth of 10-140 eV electrons in SiO_2 nanoparticles determined by Si 2p photoelectron yields, *Phys. Chem. Chem. Phys.*, 2023, **25**(22), 15173–15182, DOI: 10.1039/d3cp01284k.

35 O. Kostko, M. I. Jacobs, B. Xu, K. R. Wilson and M. Ahmed, Velocity Map Imaging of Inelastic and Elastic Low Energy Electron Scattering in Organic Nanoparticles, *J. Chem. Phys.*, 2019, **151**, 184702, DOI: 10.1063/1.5126343.

36 G. A. Garcia, L. Nahon and I. Powis, Two-dimensional Charged Particle Image Inversion Using a Polar Basis Function Expansion, *Rev. Sci. Instrum.*, 2004, **75**(11), 4989–4996, DOI: 10.1063/1.1807578.

37 H. Hertz, Ueber die Verdunstung der Flüssigkeiten, insbesondere des Quecksilbers, im luftleeren Raume, *Ann. Phys.*, 1882, **253**(10), 177–193, DOI: 10.1002/andp.18822531002.

38 M. Knudsen, Die maximale verdampfungsgeschwindigkeit des quecksilbers, *Ann. Phys.*, 1915, **352**(13), 697–708, DOI: 10.1002/andp.19153521306.

39 A. L. Buck, New Equations for Computing Vapor-Pressure and Enhancement Factor, *J. Appl. Meteorol.*, 1981, **20**(12), 1527–1532, DOI: 10.1175/1520-0450(1981)020<1527:NEFCVP>2.0.CP;2.

40 M. Faubel, S. Schlemmer and J. P. Toennies, A Molecular-Beam Study of the Evaporation of Water from a Liquid Jet, *ZPhys-e. D: At., Mol. Clusters*, 1988, **10**(2–3), 269–277, DOI: 10.1007/Bf01384861.

41 J. D. Smith, C. D. Cappa, W. S. Drisdell, R. C. Cohen and R. J. Saykally, Raman Thermometry Measurements of Free Evaporation from Liquid Water Droplets, *J. Am. Chem. Soc.*, 2006, **128**(39), 12892–12898, DOI: **10.1021/ja063579v**.

42 P. C. Chang, Y. Q. Yu, Z. H. Wu, P. C. Lin, W. R. Chen, C. C. Su, M. S. Chen, Y. L. Li, T. P. Huang, Y. Y. Lee and C. C. Wang, Molecular Basis of the Antioxidant Capability of Glutathione Unraveled via Aerosol VUV Photoelectron Spectroscopy, *J. Phys. Chem. B*, 2016, **120**(39), 10181–10191, DOI: **10.1021/acs.jpcb.6b04631**.

43 N. J. Alvarez, L. M. Walker and S. L. Anna, A Criterion to Assess the Impact of Confined Volumes on Surfactant Transport to Liquid–Fluid Interfaces, *Soft Matter*, 2012, **8**(34), 8917–8925, DOI: **10.1039/C2SM25447F**.

44 A. Bain, N. L. Prisle and B. R. Bzdek, Model-Measurement Comparisons for Surfactant-Containing Aerosol Droplets, *ACS Earth Space Chem.*, 2024, **8**(11), 2244–2255, DOI: **10.1021/acsearthspacechem.4c00199**.

45 X. L. Wang and P. H. McMurry, A Design Tool for Aerodynamic Lens Systems, *Aerosol Sci. Technol.*, 2006, **40**(5), 320–334, DOI: **10.1080/02786820600615063**.

46 T. R. Gengenbach, G. H. Major, M. R. Linford and C. D. Easton, Practical Guides for X-ray Photoelectron Spectroscopy (XPS): Interpreting the Carbon 1s Spectrum, *J. Vac. Sci. Technol., A*, 2021, **39**, 013204, DOI: **10.1116/6.0000682**.

47 Y. Liu, Is the Free Energy Change of Adsorption Correctly Calculated?, *J. Chem. Eng. Data*, 2009, **54**(7), 1981–1985, DOI: **10.1021/je800661q**.

48 P. S. Ghosal and A. K. Gupta, Determination of Thermodynamic Parameters from Langmuir Isotherm Constant-Revisited, *J. Mol. Liq.*, 2017, **225**, 137–146, DOI: **10.1016/j.molliq.2016.11.058**.

49 H. Sippola and P. Taskinen, Activity of Supercooled Water on the Ice Curve and Other Thermodynamic Properties of Liquid Water up to the Boiling Point at Standard Pressure, *J. Chem. Eng. Data*, 2018, **63**(8), 2986–2998, DOI: **10.1021/acs.jced.8b00251**.

50 T. Koop, B. P. Luo, A. Tsias and T. Peter, Water Activity as the Determinant for Homogeneous Ice Nucleation in Aqueous Solutions, *Nature*, 2000, **406**(6796), 611–614, DOI: **10.1038/35020537**.

51 S. Thürmer, R. Seidel, M. Faubel, W. Eberhardt, J. C. Hemminger, S. E. Bradforth and B. Winter, Photoelectron Angular Distributions from Liquid Water: Effects of Electron Scattering, *Phys. Rev. Lett.*, 2013, **111**(17), 173005, DOI: **10.1103/PhysRevLett.111.173005**.

52 R. Dupuy, S. Thürmer, C. Richter, T. Buttersack, F. Trinter, B. Winter and H. Bluhm, Core-Level Photoelectron Angular Distributions at the Liquid-Vapor Interface, *Acc. Chem. Res.*, 2023, **56**(3), 215–223, DOI: **10.1021/acs.accounts.2c00678**.

53 R. Dupuy, J. Filser, C. Richter, T. Buttersack, F. Trinter, S. Gholami, R. Seidel, C. Nicolas, J. Bozek, D. Egger, H. Oberhofer, S. Thürmer, U. Hergenhahn, K. Reuter, B. Winter and H. Bluhm, Ångstrom-Depth Resolution with Chemical Specificity at the Liquid-Vapor Interface, *Phys. Rev. Lett.*, 2023, **130**(15), 156901, DOI: **10.1103/PhysRevLett.130.156901**.

54 B. L. Henke, J. Liesegang and S. D. Smith, Soft-X-ray-Induced Secondary-electron Emission from Semiconductors and Insulators: Models and Measurements, *Phys. Rev. B*, 1979, **19**(6), 3004, DOI: **10.1103/PhysRevB.19.3004**.

55 J. B. Brown, Y. Q. Qian, Z. C. Huang-Fu, T. Zhang, H. Wang and Y. Rao, In Situ Probing of the Surface Properties of Droplets in the Air, *Langmuir*, 2023, **39**(31), 10724–10743, DOI: **10.1021/acs.langmuir.3c00875**.

56 Y. J. Wu, W. Y. Li, B. L. Xu, X. Li, H. Wang, V. F. McNeill, Y. Rao and H. L. Dai, Observation of Organic Molecules at the Aerosol Surface, *J. Phys. Chem. Lett.*, 2016, **7**(12), 2294–2297, DOI: **10.1021/acs.jpclett.6b00872**.

